

Entangled Radiofrequency-Photonic Sensor Network

Yi Xia^{†,1}, Wei Li^{†,2,3}, William Clark,⁴ Darlene Hart,⁵ Quntao Zhuang,^{6,1} and Zheshen Zhang^{3,1,*}

¹*James C. Wyant College of Optical Sciences, University of Arizona, Tucson, Arizona 85721, USA*

²*Department of Electronic and Information Engineering, Shanxi University, Taiyuan 030013, China*

³*Department of Materials Science and Engineering,
University of Arizona, Tucson, Arizona 85721, USA*

⁴*General Dynamics Mission Systems, 8220 East Roosevelt Street, Scottsdale, Arizona 85257, USA*

⁵*General Dynamics Mission Systems, 9 Vreeland Road, Florham Park, New Jersey 07932, USA*

⁶*Department of Electrical and Computer Engineering,
University of Arizona, Tucson, Arizona 85721, USA*

Quantum metrology [1–4] enables a measurement sensitivity below the standard quantum limit (SQL), as demonstrated in the Laser Interferometer Gravitational-wave Observatory (LIGO) [5, 6]. As a unique quantum resource, entanglement has been utilized to enhance the performance of, e.g., microscopy [7], target detection [8], and phase estimation [9]. To date, almost all existing entanglement-enhanced sensing demonstrations are restricted to improving the performance of probing optical parameters at a single sensor, but a multitude of applications rely on an array of sensors that work collectively to undertake sensing tasks in the radiofrequency (RF) and microwave spectral ranges. Here, we propose and experimentally demonstrate a reconfigurable RF-photonic sensor network comprised of three entangled sensor nodes. We show that the entanglement shared by the sensors can be tailored to substantially increase the precision of parameter estimation in networked sensing tasks, such as estimating the angle of arrival (AoA) of an RF field. Our work would open a new avenue toward utilizing quantum metrology for ultrasensitive positioning, navigation, and timing.

A variety of sensing scenarios commonly operate in the RF and microwave spectral ranges, rather than at the optical wavelengths like LIGO, thus requiring a different mechanism to achieve a quantum enhancement. In this regard, quantum illumination enables a signal-to-noise ratio (SNR) advantage over classical schemes in the RF and microwave where ambient noise is abundant [8, 10–14], but quantum illumination’s operational range and quantum enhancement are limited by large diffraction in the microwave and a lack of efficient quantum memories.

Recent advances in RF and microwave photonics [15] offer new insights for sensing. In RF-photonic sensing, RF signals are carried over to the optical domain by

electro-optic transducers (EOTs), processed by optical circuits, and measured by photodetectors. As a remarkable instance of RF-photonic sensing, a photonics-based coherent radar system has demonstrated performance metrics on par with those of state-of-the-art electronics-based radar systems [16] and further enjoys advantages in its large processing bandwidths, flexibility in engineering RF responses, and capability of transporting RF signals over long distances via optical fibers [17].

The photonic aspect of RF-photonic sensing opens a window for entanglement-enhanced performance. This paper reports a new quantum-sensing paradigm—the entangled RF-photonic sensor network—in which sensors jointly harness their shared entanglement to tackle networked RF sensing problems, such as probing the AoA of an incident RF wave, and achieve a measurement sensitivity below the SQL. Unlike quantum illumination, the entangled RF-photonic sensor network does not require quantum memories. Moreover, entangled photons are well preserved in a controlled environment to ensure large quantum-enhanced sensing performance, while the actual strong probe signals are generated by conventional RF transmitters. As such, the entangled RF-photonic sensor network is compatible with the existing RF-sensing infrastructure. By properly preparing the entanglement shared by the sensors for different sensing tasks, our entangled RF-photonic sensor network achieves an estimation variance 3.2 dB below the SQL in measuring the average field amplitudes at the sensors. In addition, we demonstrate the entangled RF-photonic sensor network’s capability of probing the AoA of an emulated incident RF wave via phase difference estimations at a central (edge) node, achieving an estimation variance 3.5 dB (3.2 dB) below the SQL.

The entangled RF-photonic sensor network is underpinned by a recent distributed quantum sensing (DQS) protocol based on continuous-variable (CV) multipartite entanglement [18]. In contrast to discrete-variable (DV) DQS [19, 20], CV-DQS features deterministic quantum-state preparation and robustness against loss. A recent proof-of-concept CV-DQS experiment showed that en-

* zsz@email.arizona.edu

[†] Equal contributions

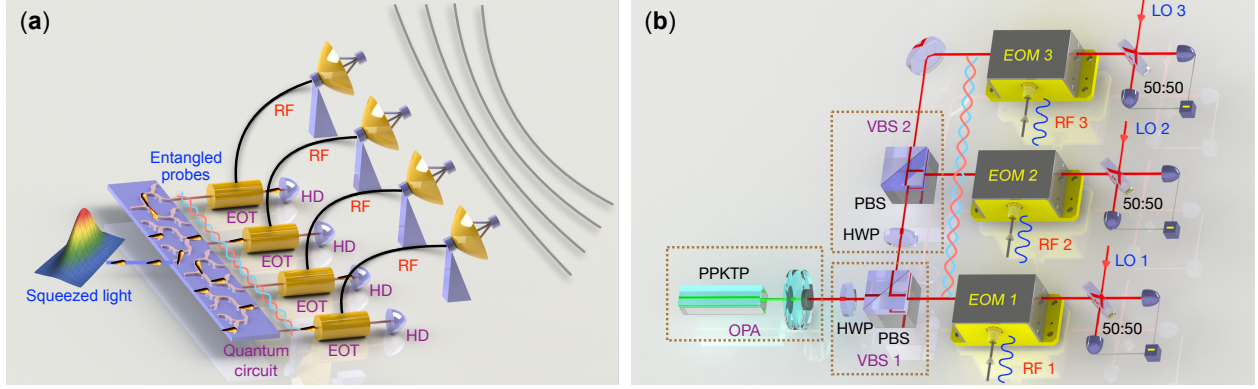


FIG. 1. (a) Concept of the entangled RF-photonic sensor network. Multiple distributed RF-photonic sensors, each consisting of an RF receiver, an electro-optic transducer (EOT), and a homodyne detector (HD), share a multipartite entangled state, generated by processing squeezed light in a quantum circuit, to enhance the performance of sensing a global property of the incident RF wave. (b) Experimental diagram. Phase squeezed light is generated from a periodically-poled KTiOPO₄ (PPKTP) crystal embedded in an optical parametric amplifier (OPA) cavity. A quantum circuit comprising two variable beam splitters (VBSs) configures the CV multipartite entangled state for three different networked sensing tasks. Each VBS consists of a half-wave plate (HWP) and a polarizing beam splitter (PBS). An RF-photonic sensor entails an electro-optic modulator (EOM) and a balanced homodyne detector supplied by a local oscillator (LO) that interferes with the quantum signal on a 50:50 beam splitter.

tanglement offers a measurement-sensitivity advantage in phase estimation over using separable states [21].

The entangled RF-photonic sensor network is conceptually illustrated in Fig. 1(a). Squeezed light with a mean photon number N_S is processed by a quantum circuit, consisting of beam splitters and phase shifters, to generate a CV multipartite entangled state tailored for a specific networked sensing task. The entangled state is then distributed to M RF-photonic sensors, each of which is equipped with an EOT. The RF field at the m -th sensor is represented by $\mathcal{E}_m(t) = E_m \cos(\omega_c t + \varphi_m)$, where ω_c is the carrier frequency, E_m is the amplitude, and φ_m is the phase of the RF field. The EOT creates a displacement

$$\alpha_m \propto E_m \sin \varphi_m \quad (1)$$

on the phase quadrature of the quantum state of light (see Appendix A for details). A homodyne detector then measures the displacement, followed by classical postprocessing on all sensors' data to estimate the probed RF-field parameter.

We aim to estimate a global property of the RF field across all sensors. Without loss of generality, let the probed global RF-field parameter tie to the weighted sum of the quadrature displacements, i.e., $\bar{\alpha} \equiv \sum_{m=1}^M v_m \alpha_m$, where the weights, $\{v_m, 1 \leq m \leq M\}$, define the global parameter estimation problem. For this purpose, the beam splitters in the quantum circuit are optimized based on the desired weights. In the absence of loss, Refs. [18, 22] present the optimum CV-DQS protocol that maximizes the quantum Fisher information. In the

presence of loss, this CV-DQS protocol remains the optimum among all protocols based on Gaussian input or homodyne measurement. The minimum estimation variance reads

$$\delta\alpha^2 = \frac{\bar{v}^2}{4} \left[\frac{\bar{\eta}}{(\sqrt{N_S} + 1 + \sqrt{N_S})^2} + 1 - \bar{\eta} \right], \quad (2)$$

where $\bar{v} \equiv \sqrt{\sum_{m=1}^M v_m^2}$, $\bar{\eta} \equiv \sum_{m=1}^M v_m^2 \eta_m / \bar{v}^2$, and $1 - \eta_m$ is the loss at the m -th sensor. At $\eta_m = 1$ and a fixed mean photon number $n_s \equiv N_S / M$ at each sensor, equal weights yield $\delta\alpha^2 \propto (1/M)^2 \times 1/n_s$, i.e., a Heisenberg scaling for estimation variance with respect to the number of sensors, whereas any protocol without entanglement is subject to the SQL. Also, $M = 1$ reduces the situation to single parameter estimation enhanced by a single-mode squeezed vacuum state, with $\bar{v} = 1$ and $\bar{\eta} = \eta$ being the single-mode loss. It is worth emphasizing that, unlike DV-DQS protocols, the advantage of the CV-DQS protocol over classical schemes survives loss, even though loss precludes a Heisenberg scaling.

The experiment is illustrated in Fig. 1(b). Phase squeezed state, generated from an optical parametric amplifier (OPA), is processed by a quantum circuit, comprised of two variable beam splitters (VBSs), to produce a CV multipartite entangled state shared by three RF-photonic sensors. At each sensor, an electro-optic modulator (EOM) driven by the probed RF field induces a displacement on the squeezed phase quadrature (see Meth-

ods), as described by Eq. 1. To estimate the displacement, a local oscillator (LO) interferes with the signal on a 50:50 beam splitter to carry out a balanced homodyne measurement. The time-domain data from the three homodyne measurements are postprocessed to derive the estimated parameter and the associated estimation variance under different configurations.

Prior to constructing an entangled sensor network, we first assess RF-photonic sensing enhanced by single-mode squeezed light. To do so, VBS 1 is configured to deliver all light to Sensor 1. Fig. 2 (inset) first plots in the gold curve the calibrated shot-noise level with its standard deviation normalized to 1 to represent the SQL. The blue and red curves are, respectively, the traces at $\varphi_1 = 0.54\pi$ and 1.32π and are normalized using the same factor as that of the gold curve. The standard deviations of the curves reflect the quantum measurement noise, which in turn determines the estimation variance. Beating the SQL is a nonclassical characteristic, as witnessed in the standard deviations of the red and blue curves. Both cases suppress the SQL by ~ 4 dB. The means of the time-domain homodyne traces, as the phase of the RF signal is swept, are then scaled to the SQL unit and plotted as red circles in Fig. 2, showing a nice fit to a sinusoidal function, as expected.

We now demonstrate the power of CV multipartite en-

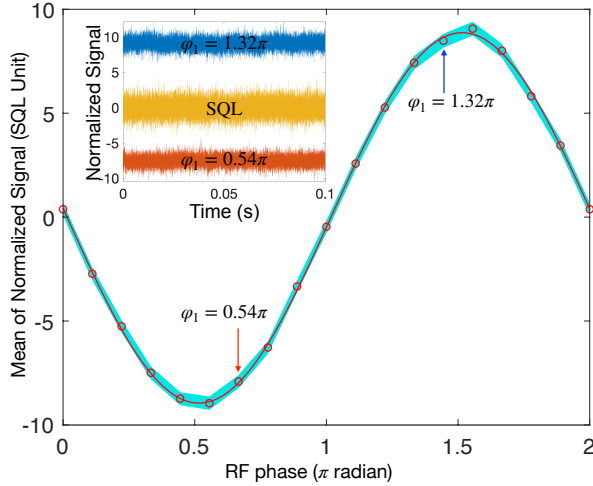


FIG. 2. Means of the homodyne output at different RF phases. The shot-noise limit dictates the SQL and is normalized to a standard deviation of 1. All signals are normalized using the same factor for the SQL normalization. Circles: experimental measurements; red curve: sinusoidal fit; shaded area: normalized standard deviation of the measurement noise. (inset) Time-domain traces of the homodyne output at $\varphi_1 = 0.54\pi$ (red) and 1.32π (blue) as compared to the SQL (gold), showing a 4-dB noise reduction.

tanglement in three networked sensing tasks. First, the average RF-field amplitude at the three sensors is estimated using an equally weighted CV multipartite entangled state, which yields the optimum performance (see Appendix A). The RF-field amplitude at Sensor 1 is swept from 20 mV to 160 mV while keep the amplitudes of Sensor 2 and 3 at 80 mV. The homodyne data from the three sensors are first averaged and then scaled to ensure an unbiased estimator. The estimates are plotted as blue circles in Fig. 3(a), with the blue shaded area representing the estimation uncertainty due to quantum measurement noise. As a comparison, the estimated average RF-field amplitudes by a classical separable sensor network are plotted as red triangles in the same figure, with the red shaded area representing the estimation uncertainty. The entangled sensor network shows a reduced estimation variance of 3.2 dB in this sensing scenario.

We then estimate the AoA of an emulated incident RF field. In a one-dimensional sensor array, this sensing problem is translated into the estimation of the phase difference across the sensors, which can be solved by a finite difference method (see Appendix A 4). To estimate the phase difference at a central node, the weights for the optimum CV multipartite entangled state is $[1/2, 0, -1/2]$, generated by setting the splitting ratios of VBS 1 and 2 to 1:1 and 0:1. The AoA is emulated by an RF-field phase difference across the three sensors. The negative sign in the weight is introduced by adding a π -phase delay at Sensor 3. In the measurement, the RF phase at Sensor 1 is swept from 0.17 rad to -0.17 rad, and at the same time the RF phase at Sensor 2 is swept from -0.17 rad to 0.17 rad, while RF-field amplitudes are set identical. The homodyne data from the three sensors are weighted to obtain an unbiased estimator. The estimated phase difference vs. the applied RF-field phase are plotted as blue circles in Fig. 3(b) and compared to the classical separable scheme (red triangles), with the shaded area representing the estimation uncertainties, showing a 3.5-dB reduction for the entangled case.

We last estimate the RF-field phase difference at an edge node. The optimum weights of the CV multipartite entangled state for this problem are $[-3/2, 2, -1/2]$, generated by setting the splitting ratios of the VBSs to 1:1 and 3:1. In this measurement, the RF phase at Sensor 2 and 3 is swept from -0.17 rad to 0.17 rad while the RF phase at Sensor 2 is set to 0. The estimated phase difference vs. the applied RF-field phase are plotted in Fig. 3 (c) for the entangled scheme (blue circles) and compared to that of the classical separable scheme (red triangles) networks, showing a 3.2-dB reduction in the estimation variance.

While quantum noise arises in each homodyne measurement, a proper multipartite entangled state leads to a reduction in the overall estimation variance, whereas

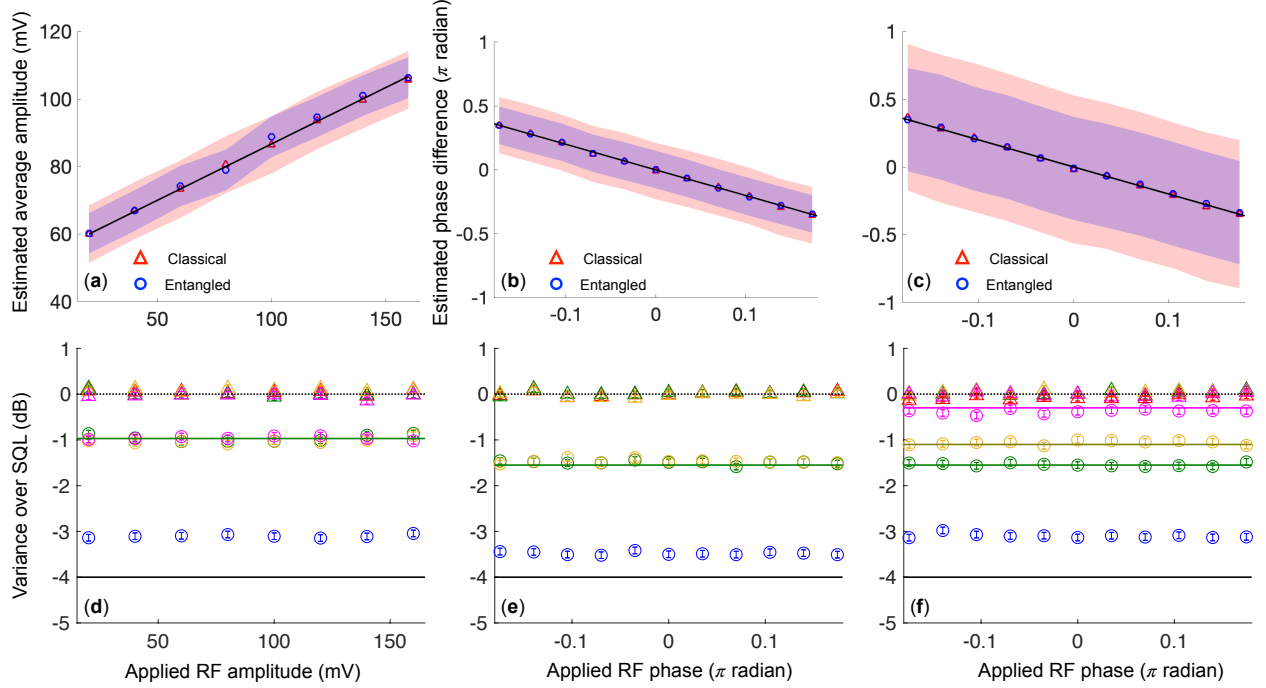


FIG. 3. Estimation of (a) average field amplitude; (b) phase difference at a central node; and (c) phase difference at an edge node. Noise variances at (d) different field amplitudes; (e) different phase differences at a central node; and (f) at different phase differences at an edge node. Shaded area: estimation uncertainties for the entangled (blue) and classical separable (red) sensor networks. The entangled sensors show a clear reduced estimation uncertainty. In (d), (e), (f), measurement noise variances are plotted in green for Sensor 1, gold for Sensor 2, and magenta for Sensor 3. Estimation variances, normalized to the SQL, for entangled (blue) and classical separable (red) sensor networks. Circles: data for entangled sensors; triangles: data for classical separable sensors. Green, gold, and magenta solid horizontal lines: theory curves for noise variances at three sensors. Solid black horizontal line: ideal estimation variance for entangled sensors; experimental deviation likely caused by imperfect phase locking between sensors. Dotted black horizontal line: the SQL for measurement noise variances and normalized estimation variances. While all classical data stay at the SQL, the estimation variances for the entangled sensor networks are sub-SQL and are significantly lower than the measurement noise variances at single sensors. Error bars reflect estimated measurement uncertainties caused by system instabilities.

such an noise reduction mechanism is absent in a classical separable sensor network. Figure 3 (d), (e), (f) show such a behavior. The measurement noise variances at the three sensors, represented by green, gold, and magenta, are plotted for both the entangled (circles) and classical separable (triangles) cases in the SQL unit. To facilitate the comparison, the estimation variances for the three tasks are also normalized to the SQL using a factor predetermined by the weights and are depicted as blue circles and red triangles for, respectively, the entangled and classical separable cases. It is evident that all classical data stay at the SQL. For the entangled sensor network, while the noise variances at each sensor barely suppresses the SQL by ~ 0.3 dB to 1.5 dB, the normalized estimation variances, however, substantially beats the SQL by 3.2 ± 0.1 dB, 3.5 ± 0.1 dB, and 3.2 ± 0.1 dB in the three sensing tasks.

A unique aspect of an entangled sensor network is that

a proper multipartite entangled state need be prepared to achieve the optimum performance in a specific networked sensing task. To show this, the splitting ratios for the VBSs are varied to prepare different entangled states for each of the three sensing tasks, and the resulting estimation variances are compared with those of a classical separable sensor network under the same VBS settings. The tuning ranges of the VBS splitting ratios for the three sensing tasks are described in the insets of Fig. 4. In the measurements, a negative splitting ratio indicates a π -phase shift on the the RF signal at a sensor, which can be effectively viewed as a π -phase shift on its received entangled state (see Methods). For each sensing task, the homodyne data are first scaled and added up to ensure an unbiased estimator. The estimation variances are then normalized to the SQL and are plotted in Figs. 4(a), 4(b), and 4(c), showing excellent agreement with theory.

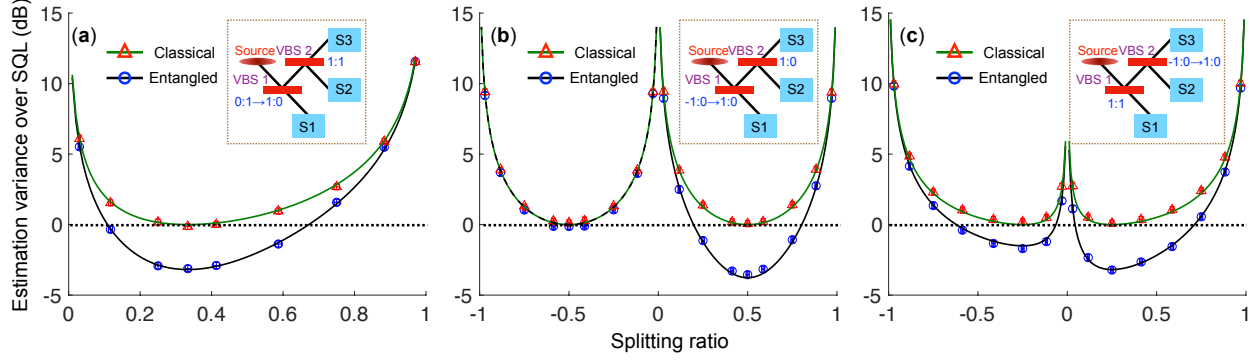


FIG. 4. Optimization of CV multipartite entangled state for the three sensing tasks: estimation of (a) average RF-field amplitude; (b) phase difference at a central node; and (c) phase difference at an edge node. Circles: entangled sensors data; triangles: classical separable sensors data; black curves: quantum theory; green curves: classical theory. Black horizontal dotted line: the SQL. Error bars account for estimated uncertainties arising from experimental instabilities. The symmetric classical curves vs. the asymmetric quantum curves in (b) and (c) manifest the correlated quantum noise arising from the homodyne detectors at different sensors. Insets: illustration of the tuning ranges of the VBS splitting ratios. S: Sensor.

The estimation variance vs. splitting ratio curves for phase-difference estimations, plotted in Figs. 4(b) and 4(c), show very different behaviors for the entangled and classical separable cases. The curves for the classical separable case are symmetric, with the minimum estimation variances found at both positive and negative splitting ratios, whereas the curves for the entangled case display a strong asymmetric characteristic. Such a behavior manifests the entanglement shared by the sensors. In a classical separable sensor network, the quantum fluctuations are independent at different sensors, so postprocessing on the measurement data to acquire an unbiased estimator does not alter the noise power. In an entangled sensor network, however, the quantum fluctuations at different sensors are correlated, so the measurement noise can only be reduced to minimum if the homodyne data from different sensors are added up with a proper set of weights. Importantly, these weights also need to ensure an unbiased estimator. As such, tailoring a proper CV multipartite entangled state for a specific networked sensing problem to simultaneously satisfy the two criteria is critical to achieve a large quantum advantage over a classical separable sensor network.

Before closing, a few remarks are worth making. The magnitude of the quadrature displacement is proportional to the RF-to-photon conversion efficiency determined by the V_π of the EOM. Our free-space EOM's $V_\pi \approx 350$ V leads to a low conversion efficiency. The V_π 's for integrated EOTs can be substantially reduced, as recently demonstrated in Ref. [23].

The phase squeezed state at the source is Gaussian. Since only Gaussian operations are performed, the entangled state shared by the sensors remains Gaussian.

Ref. [18] proved that the optimum separable state for the CV-DQS protocol, subject to the photon-number constraint, is a product of three single-mode squeezed vacuum state, and the minimum estimation variance is achieved by homodyne measurements. Appendix. A 3 shows that the measured estimation variance beats that of the optimum separable state by $\sim 10\%$, thereby verifying that quantum state is entangled. A similar tool has recently been developed to characterize Gaussian multipartite entanglement [24].

While the entangled RF-photon sensor network, in its present form, cannot beat the ultimate AoA estimation precision limit set by the RF sky temperature, it does offer an advantage over a classical RF-photon sensor network undertaking the same sensing task, as long as sensors are situated within a few kilometers apart in a controlled local environment so that low-loss optical fibers can be utilized to distribute entanglement without significant loss penalty. The outputs from the EOMs can also be collected and sent, via optical fibers, to a central location for additional quantum processing prior to the measurements [25]. To further enlarge the distances between entangled sensors, techniques like noiseless linear amplifiers [22, 26] and CV error correction [27] can be used to overcome loss and achieve an entanglement-enhanced performance. Also, the number of sensors can be scaled up by splitting the multipartite entangled state into more arms.

In conclusion, we implemented a three-node entangled RF-photon sensor network and demonstrated sub-SQL estimation variances in networked sensing tasks, including the estimation of the average amplitudes and AoA of an RF field. In optimizing the CV multipartite

tite entangled state for different sensing tasks, nonclassical quantum noise reduction was observed. This new quantum-sensing paradigm would create opportunities for the next-generation ultrasensitive position, navigation, timing, and imaging applications.

METHODS

Experiment

Phase squeezed state is produced from an optical parametric amplifier (OPA) seeded with weak coherent light and locked, using a 20-MHz sideband signal, to operate in a parametric amplification regime. The squeezed light for RF sensing resides at sidebands 11-MHz detuned from the baseband light. The sideband detuning matches the RF-field carrier frequency ω_c . The squeezed light is then processed by a reconfigurable quantum circuit comprised of two variable beam splitters (VBSs), each of which consists of a half-wave plate (HWP) followed by a polarizing beam splitter (PBS). One output signal of VBS 1 goes to Sensor 1, while the other output undergoes VBS 2. The two outputs of VBS2 are then diverted to Sensor 2 and 3. The RF-photonic sensor is realized by an electro-optic modulator (EOM), which is driven by the probed RF field at a carrier frequency of 11 MHz to induce a field quadrature displacement at the signal's 11-MHz sidebands that accommodate the squeezed light (see Appendix B). The magnitude of the displacement is determined by the amplitude and phase of probed RF field, as shown in Eq. 1. In the homodyne measurement, a local oscillator (LO) interferes with the signal on a 50:50 beam splitter, whose two output arms are detected by two photodiodes each with $\sim 88\%$ quantum efficiency. The DC component of the difference photocurrent of the two photodiodes provides an error signal that is fed back to a piezoelectric transducer to lock the phase between the LO and the signal so that the LO precisely addresses the squeezed quadrature in the displacement measurement. The probed properties of the RF field are now carried on the 11-MHz component of the difference photocurrent, which is subsequently demodulated by an electronic mixer and then filtered by a 240-kHz low-pass filter. The homodyne data collected at the three sensors are recorded by an oscilloscope with 4-GHz analog bandwidth and 50 M Samples/s/channel sampling rate. The estimation variances under different configurations are obtained in post data-processing on the acquired digital data.

Theory

In the entangled RF-photonic sensor network, let the global parameter to be estimated be a weighted average of the phase of the RF field at different sensors, i.e., $\bar{\varphi} = \sum_m c_m \varphi_m$, with the weights c_m 's being real. Also the estimation of any analytical function of φ_m 's can be reduced to the estimation of weighted sum by linearization and adopting adaptivity [29]. The average field-amplitude estimation problem can be formulated in a similar way. Under beam splitter ratios $\{w_m\}$ for amplitude and $\{g_m = \pm 1\}$ determined by RF phase delays at the sensors, the estimation variance can be derived as

$$\text{var} = \frac{1}{\beta^2} \left[\left(\sum_{m=1}^M g_m c_m \right)^2 \delta_b + \frac{1}{4} \left(\sum_{m=1}^M \frac{c_m^2}{w_m^2} \right) \right].$$

Here, β is a coefficient determined by the mean photon number of the baseband light, the transduction efficiency of the EOM, and the system efficiency. $\delta_b \equiv \eta \langle \text{Im} [\hat{b}]^2 \rangle - \eta/4$, with $\langle \text{Im} [\hat{b}]^2 \rangle$ being the variance of the phase squeezed state at the source (shot-noise variance is $1/4$) and $1 - \eta$ being the overall loss seen by each sensor. $\delta_b = 0$ in the classical separable case and $\delta_b < 0$ in the entangled case. The optimum parameter choices are thus $w_m^{\text{opt}} = \sqrt{|c_m|} / \sqrt{\sum |c_m|}$ and $g_m^{\text{opt}} = \text{sign}(c_m)$, leading to a minimum estimation variance $(\sum |c_m|)^2 \langle \text{Im} [\hat{b}]^2 \rangle / \beta^2$ (refer to Appendix A for derivation details).

The above result is used to model the experimental data in Fig. 4. To facilitate the comparison, the minimum estimation variance of a classical separable sensor network, $(\sum |c_m|)^2 / (4\beta^2)$, is set as the SQL. In Fig. 3 (d)–(f) and Fig. 4, the estimation variances are normalized to the SQL unit. The estimation of the average RF-field amplitude requires $c_1 = c_2 = c_3 = 1/3$ and $g_1 = g_2 = g_3 = 1$. In the experiment, the splitting ratio of VBS 1, r , is tuned from 0:1 to 1:0 while the splitting ratio of VBS 2 is kept 1:1, so that $w_1 = \sqrt{r}$, $w_2 = w_3 = \sqrt{(1-r)/2}$. This leads to $\text{var} = (1/\beta^2)(\delta_b + [1/(1-r) + 1/4r]/9)$, with the minimum achieved at $r = 1/3$. The theory and the experimental data are plotted in Fig. 4(a), showing excellent agreement. To estimate the phase difference at a central node, we set $c_1 = 1/2$, $c_2 = 0$, $c_3 = -1/2$. The splitting ratio of VBS 1, r , is tuned between -1:0 and 1:0 while the splitting ratio of VBS 2 is kept 1:0, corresponding to $w_1 = \sqrt{|r|}$, $w_2 = 0$, $w_3 = \sqrt{1-|r|}$ and $g_1 = \text{sign}(r)$, $g_2 = 1$, $g_3 = -1$. Here, $g_m = -1$ indicates a π -phase shift on the RF field probed by the m -th sensor, which can be effectively viewed as applying a π -phase shift on its received entangled state while ensuring an unbiased estimator. For $r > 0$, $\text{var}_+ = (1/\beta^2)(\delta_b + [1/(1-r) + 1/r]/16)$, which is minimized at

$r = 1/2$, as seen in the right half of Fig. 4(b). We then set $r < 0$, leading to $\text{var}_- = (1/\beta^2)[1/(1-|r|) + 1/|r|]/16$. Since δ_b is absent in var_- , the estimation variances for the entangled and classical separable cases are identical and are both minimized at $r = -1/2$, as shown in the left half of Fig. 4(b). The estimation of the phase difference at an edge node requires $c_1 = 2, c_2 = -3/2, c_3 = -1/2$. The splitting ratio of VBS 1 is kept 1:1 while the splitting ratio VBS 2, r , is tuned between -1:0 and 1:0, corresponding to $w_1 = \sqrt{1/2}, w_2 = \sqrt{(1-|r|)/2}, w_3 = \sqrt{|r|/2}$ and $g_1 = 1, g_2 = -1, g_3 = -\text{sign}(r)$. We first set $r > 0$, leading to $\text{var}_+ = (1/\beta^2)(16\delta_b + [8 + 9/2(1-r) + 1/2r]/4)$, which is plotted with the experimental data in the right half of Fig. 4(c). The minimum estimation variance is achieved at $r = 1/4$. We then set $r < 0$, leading to $\text{var}_- = (1/\beta^2)(9\delta_b + [8 + 9/2(1-|r|) + 1/2|r|]/4) > \text{var}_+$, as plotted with the experimental data in the left half of Fig. 4(c). The minimum estimation variance is achieved at $r = -1/4$.

ACKNOWLEDGMENTS

This work is funded by General Dynamics Mission Systems. We thank General Dynamics Mission Systems, the Office of Naval Research, and the University of Arizona for their support in quantum research.

AUTHOR CONTRIBUTIONS

Z.Z. initiated the experiment. Q.Z. formulated the theoretical framework. Y.X. and W.L. built the experimental setup and acquired the data. W.C. and D.H. contributed to system-level analysis. All authors are involved in analyzing the experimental data or interpreting the results. Z.Z. and Q.Z. wrote the initial manuscript with inputs from all others.

Appendix A: Theoretical Framework

1. Single RF-photon sensor enhanced by squeezed light

We consider an entangled RF-photon sensor network composed of M sensors. The quantum states of interest at each sensor are carried on three optical spectral modes, i.e., a central mode $\hat{a}_c^{(m)}$ at the optical carrier frequency Ω and two sideband modes $\hat{a}_\pm^{(m)}$ at optical frequencies $\Omega \pm \omega_c$. Here, $1 \leq m \leq M$ indexes the sensors. Suppose the probed RF field at the m -th sensor is represented by the waveform $\mathcal{E}_m(t) = E_m \cos(\omega_c t + \varphi_m)$, where ω_c is the carrier frequency of the RF field, E_m is the RF-field

amplitude, and φ_m is the RF-field phase. The EOM transduces the RF field into a phase modulation on the optical field so that the spectral mode $\hat{a}_\omega e^{-i\omega t}$ at ω becomes

$$\hat{a}_\omega e^{-i\omega t} e^{i\zeta E_m \cos(\omega_c t + \varphi_m)} = \hat{a}_\omega \sum_{n=-\infty}^{\infty} i^n J_n(A_m) e^{i(-(\omega - n\omega_c)t + n\varphi_m)}, \quad (\text{A1})$$

where the Jacobi-Anger expansion has been employed, $J_n(z)$ is the n -th Bessel function of the first kind. Here $A_m = \zeta E_m$, where $\zeta = \pi/V_\pi$ accounts for the RF-to-photon conversion efficiency. Effectively, the spectral mode \hat{a}_ω undergoes a frequency-domain beam splitter transform and is spread over to the spectral modes $\omega - n\omega_c, n = 0, \pm 1, \pm 2, \dots$. For small A_m , $J(A_m) \sim (A_m)^n 2^{-n}/n!$ decays quickly with n . In a weak RF-field scenario, only the $n = 0, \pm 1$ components need be considered such that $\hat{a}^{(m)}$'s undergo an effective frequency-domain beam splitter transform, yielding the transformed spectral mode operators

$$\begin{aligned} \hat{a}_c^{(m)'} &= J_0(A_m)\hat{a}_c^{(m)} + iJ_1(A_m)\hat{a}_-^{(m)} e^{i\varphi_m} + iJ_1(A_m)\hat{a}_+^{(m)} e^{-i\varphi_m} \\ \hat{a}_+^{(m)'} &= J_0(A_m)\hat{a}_+^{(m)} + iJ_1(A_m)\hat{a}_c^{(m)} e^{i\varphi_m} + iJ_1(A_m)\hat{a}_{2+}^{(m)} e^{-i\varphi_m} \\ \hat{a}_-^{(m)'} &= J_0(A_m)\hat{a}_-^{(m)} + iJ_1(A_m)\hat{a}_{2-}^{(m)} e^{i\varphi_m} + iJ_1(A_m)\hat{a}_c^{(m)} e^{-i\varphi_m}, \end{aligned} \quad (\text{A2})$$

where $\hat{a}_{2\pm}^{(m)}$ are higher-order spectral modes at frequencies $\Omega \pm 2\omega_c$, and $J_{-n}(z) = (-1)^n J_n(z)$ has been used. Initially, all the sideband modes $\hat{a}_\pm^{(m)}, \hat{a}_{2\pm}^{(m)}$ are in zero-mean states, while the central spectral mode $\hat{a}_c^{(m)}$ is in a quantum state close to the coherent state $|\alpha_m\rangle$. Thus, $\langle \hat{a}_\pm^{(m)} \rangle = iJ_1(A_m)e^{\pm i\varphi_m} \alpha_m$.

The optical field operator carrying the three spectral modes at sensor m now reads

$$\hat{E}^{(m)}(t) = \hat{a}_c^{(m)'} e^{-i\Omega t} + \hat{a}_+^{(m)'} e^{-i(\Omega + \omega_c)t} + \hat{a}_-^{(m)'} e^{-i(\Omega - \omega_c)t}. \quad (\text{A3})$$

Let the LO optical field be $E_{\text{LO}}^{(m)}(t) = E_{\text{LO}} e^{-i(\Omega t + \theta)}$, where E_{LO} is real. The balanced homodyne measurement generates a photocurrent

$$\begin{aligned} I(t) &= \text{Re} [\hat{E}^{(m)} E_{\text{LO}}^{(m)*}] \\ &= \text{Re} [E_{\text{LO}} e^{i\theta} (\hat{a}_c^{(m)'} + \hat{a}_+^{(m)'} e^{-i\omega_c t} + \hat{a}_-^{(m)'} e^{i\omega_c t})], \end{aligned} \quad (\text{A4})$$

where we have set the electron charge $q = 1$ for theoretical convenience.

An electronic mixer supplied by an RF LO at ω_c and with a phase ϕ_0 is then applied on the photocurrent, i.e. $\cos(\omega_c t + \phi_0)$, moving the photocurrent's spectral component at ω_c to the baseband. After filtering, the baseband photocurrent reads

$$I_B^{(m)}(t) = -\text{Re} [e^{i\theta} \hat{b}^{(m)'}], \quad (\text{A5})$$

where we have defined the mode

$$\hat{b}^{(m)'} \equiv (e^{i\phi_0} \hat{a}_+^{(m)'} + e^{-i\phi_0} \hat{a}_-^{(m)'}) / \sqrt{2}. \quad (\text{A6})$$

In doing so, one only needs to consider measurements on the effective mode $\hat{b}^{(m)'}$ in estimating the parameters of the probed RF field. Likewise, a corresponding effective mode before the RF-to-phonic transduction is defined as

$$\hat{b}^{(m)} \equiv (e^{i\phi_0} \hat{a}_+^{(m)} + e^{-i\phi_0} \hat{a}_-^{(m)}) / \sqrt{2}. \quad (\text{A7})$$

Derived from Eq. A2, the transform of the effective mode through the transduction is

$$\hat{b}^{(m)'} = J_0(A_m) \hat{b}^{(m)} + i \sqrt{2} J_1(A_m) \cos(\phi_0 + \varphi_m) \hat{a}_c^{(m)} + \text{v.c.}, \quad (\text{A8})$$

where v.c. are the vacuum modes and higher order zero-mean modes. For $A_m \ll 1$ and $|\alpha_m| \gg 1$, the evolution of \hat{b}_m through the transduction is well described by a first-order approximation, giving a displacement of $i \sqrt{2} J_1(A_m) \cos(\phi_0 + \varphi_m) \alpha_m$ on \hat{b}_m on the phase quadrature. Thus, to access the displacement, the LO phase needs to be set to $\theta = \pi/2$ to observe the phase quadrature of $\hat{b}^{(m)}$, i.e., $I_B^{(m)}(t) = \text{Im}[\hat{b}^{(m)'}]$, as experimentally verified by the sinusoidal signal in Fig. 2. Moreover, because the RF-field information is transferred to the phase quadrature of the effective mode, a quantum enhancement in the measurement sensitivity requires that the effective mode is in a phase squeezed state. This is achieved by setting the OPA to operate in a parametric amplification regime.

To measure a RF-field phase $\varphi_m \ll 1$, we set $\phi_0 = \mp \pi/2$, then the effective mode, up to the leading order, becomes

$$\hat{b}^{(m)'} = J_0(A_m) \hat{b}^{(m)} + g_m i \sqrt{2} J_1(A_m) \varphi_m \hat{a}_c^{(m)} + \text{v.c.}, \quad (\text{A9})$$

where $g_m = \pm 1$ can be tuned by the sign of ϕ_0 .

2. Entangled RF-phonic sensor network

Shown in Fig. 5, to apply the DQS protocol developed in Ref. [18] to an entangled RF-phonic sensor network, the quantum source first effectively generates a single-mode squeezed vacuum mode $\hat{b} = i(\hat{a}_+ - \hat{a}_-) / \sqrt{2}$, where \hat{a}_\pm are the sideband modes. Subsequently, a beam splitter array with weights $\{w_m, 1 \leq m \leq M\}$ ($\sum w_m^2 = 1$) produces the modes $\hat{b}^{(m)} = i(\hat{a}_+^{(m)} - \hat{a}_-^{(m)}) / \sqrt{2}$ that are distributed to different sensors. In the experiment, such a state is produced a two-mode squeezed vacuum state between the sideband modes \hat{a}_\pm such that $\langle \hat{a}_+ \hat{a}_- \rangle = \sqrt{N_S(N_S + 1)} e^{i\tau}$ and $\langle \hat{a}_+^2 \rangle = \langle \hat{a}_-^2 \rangle = 0$, where N_S is the

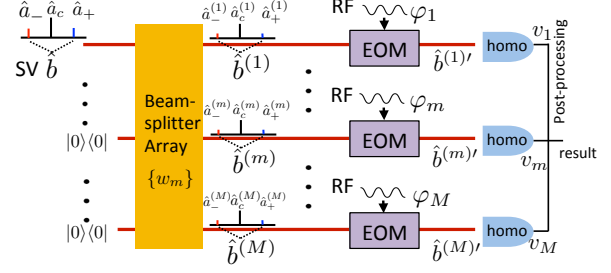


FIG. 5. Theoretical model for the entangled RF-phonic sensor network. SV: squeezed vacuum. EOM: electro-optic modulator. homo: homodyne measurement. At the quantum source, the sideband modes \hat{a}_\pm are entangled in a two-mode squeezed state, leading to the effective mode $\hat{b} = i(\hat{a}_+ - \hat{a}_-) / \sqrt{2}$ in a phase SV state. The central spectral mode \hat{a}_c is close to a coherent state $|\alpha\rangle$. A beam splitter array with weights $\{w_m, 1 \leq m \leq M\}$ generates the CV multipartite entangled state of the effective modes $\{\hat{b}^{(m)}, 1 \leq m \leq M\}$. Each $\hat{b}^{(m)} = i(\hat{a}_+^{(m)} - \hat{a}_-^{(m)}) / \sqrt{2}$ accounts for two sideband modes. The EOM transduces the RF signal into optical field quadrature displacements. Postprocessing of homodyne measurement results at all sensors generates a sum with weights $\{v_m, 1 \leq m \leq M\}$, which is used to infer the average RF-field amplitude or the AoA.

mean photon number. The variance of the phase quadrature $\langle \text{Im}[\hat{b}]^2 \rangle = (2N_S + 1 - 2 \cos \tau \sqrt{N_S(N_S + 1)})/4$. Choosing $\tau = 0$, the variance is minimized to

$$\langle \text{Im}[\hat{b}]^2 \rangle = \frac{1}{4} \frac{1}{(\sqrt{N_S} + \sqrt{N_S + 1})^2}, \quad (\text{A10})$$

so that a squeezed vacuum state is generated at the effective mode \hat{b} .

In the beam splitter array, all spectral modes undergo the same transform. Thus, the central spectral modes $\hat{a}_c^{(m)}$ at different sensors are also generated by splitting the central spectral mode \hat{a}_c at the source. Prior to the EOM at each sensor, $\hat{b}^{(m)} = w_m \hat{b} + \text{v.c.}$, $\hat{a}_c^{(m)} = w_m \hat{a}_c + \text{v.c.}$, and the effective mode after the EOM becomes

$$\hat{b}^{(m)'} = J_0(A_m) w_m \hat{b} + g_m w_m i \sqrt{2} J_1(A_m) \varphi_m \hat{a}_c + \text{v.c.}, \quad (\text{A11})$$

on which the phase quadrature $I_B^{(m)}(t) = \text{Im}[\hat{b}^{(m)'}]$ is measured.

Suppose the global parameter to be estimated is $\bar{\varphi} = \sum_m c_m \varphi_m$, with weights being c_m real. To obtain an estimation, a suitable set of w_m 's is required, and postprocessing on measurement outcomes of all sensors is fur-

ther needed to construct an unbiased estimator

$$\hat{L} = s \sum_m v_m I_B^{(m)}(t) = s \text{Im} \left[\sum_m v_m \hat{b}^{(m)\prime} \right], \quad (\text{A12})$$

where the weights v_m are real and normalized, $\sum_m v_m^2 = 1$, and $s > 0$ is a scaling factor. The unbiased condition requires the expectation value

$$\langle \hat{L} \rangle = s \sum_m v_m g_m w_m \varphi_m \beta = \sum_m c_m \varphi_m, \quad (\text{A13})$$

where $\sqrt{2}J_1(A_m)\alpha = \beta$ is fixed. Thus, the chosen v_m, w_m 's need to make $c_m = s g_m v_m w_m \beta, \forall m$.

To use the phase squeezed state in the \hat{b} mode to minimize the variance of the estimator, $v_m = w_m$ is needed, and consequently the optimum choices of the parameters are

$$w_m^{\text{opt}} = \frac{\sqrt{|c_m|}}{\sqrt{\sum |c_m|}}, g_m^{\text{opt}} = \text{sign}(c_m), s^{\text{opt}} = \sum |c_m|/\beta. \quad (\text{A14})$$

The minimum variance is thus

$$\text{var}(\hat{L})^{\text{opt}} = \left(\sum |c_m|/\beta \right)^2 \langle \text{Im}[\hat{b}]^2 \rangle, \quad (\text{A15})$$

where the variance of the phase squeezed state is given by Eq. A10.

To show that the weights w_m^{opt} 's indeed yield the optimum entanglement-enhanced estimation performance, we choose a set of sub-optimum beam splitter ratios $\{w_m, 1 \leq m \leq M\}$ and the associated postprocessing weights $\{v_m, 1 \leq m \leq M\}$ to maintain an unbiased estimator, as specified in Eq. A13. The estimator variance is then derived as following. Denote the effective modes as $\hat{b}' = (\hat{b}^{(1)\prime}, \dots, \hat{b}^{(M)\prime})^T$, obtained from a beam splitter transform $\mathbf{T} = (\mathbf{w}, \mathbf{T}_1)$ on mode \hat{b} and vacuum modes $\hat{e} = (\hat{e}_2, \dots, \hat{e}_M)$. Here, $\mathbf{w} \equiv (w_1, \dots, w_M)^T$, i.e., $\hat{b}' = (\mathbf{w}, \mathbf{T}_1)(\hat{b}, \hat{e})^T$. From the orthogonality condition, $\mathbf{T}^T \mathbf{T} = \mathbf{T} \mathbf{T}^T = \mathbf{I}_M$, one has $\mathbf{w}^T \mathbf{w} = 1, \mathbf{w}^T \mathbf{T}_1 = 0, \mathbf{T}_1^T \mathbf{T}_1 = \mathbf{I}_{M-1}$, and $\mathbf{w} \mathbf{w}^T + \mathbf{T}_1 \mathbf{T}_1^T = \mathbf{I}_{M-1}$. Here, \mathbf{I}_L is an $L \times L$ identity matrix. Let $\mathbf{v} = (v_1, \dots, v_M)^T$, the estimator is then written as $\hat{L} = s \text{Im}[\mathbf{v}^T \mathbf{T}(\hat{b}, \hat{e})^T]$. Thus,

the variance of the estimator

$$\begin{aligned} \text{var}(\hat{L}) &= s^2 \mathbf{v}^T \mathbf{T} \text{Diag} \left[\langle \text{Im}[\hat{b}]^2 \rangle, \frac{1}{4} \mathbf{I}_{M-1} \right] \mathbf{T}^T \mathbf{v} \\ &= s^2 (\mathbf{v}^T \mathbf{w})^2 \langle \text{Im}[\hat{b}]^2 \rangle + \frac{1}{4} s^2 \mathbf{v}^T \mathbf{T}_1 \mathbf{T}_1^T \mathbf{v} \\ &= s^2 (\mathbf{v}^T \mathbf{w})^2 \left(\langle \text{Im}[\hat{b}]^2 \rangle - \frac{1}{4} \right) + \frac{1}{4} s^2 \mathbf{v}^T \mathbf{v} \\ &= \frac{1}{\beta^2} \left[\left(\sum_{m=1}^M g_m c_m \right)^2 \left(\langle \text{Im}[\hat{b}]^2 \rangle - \frac{1}{4} \right) + \frac{1}{4} \left(\sum_{m=1}^M \frac{c_m^2}{w_m^2} \right) \right], \end{aligned} \quad (\text{A16})$$

where $\mathbf{v}^T \mathbf{w} = \sum_{m=1}^M g_m c_m / s \beta$ and $\mathbf{v}^T \mathbf{v} = \sum_{m=1}^M c_m^2 / (s^2 w_m^2 \beta^2)$ have been used. Again, the variance of the phase squeezed state is given in Eq. A10. To rederive the optimum parameters w_m 's and g_m 's, the constraint $\sum_{m=1}^M w_m^2 = 1$ is considered. Using Lagrangian multipliers, it becomes easy to see that $w_m \propto \sqrt{|c_m|}$. Also, since $\langle \text{Im}[\hat{b}]^2 \rangle - \frac{1}{4} \leq 0$ due to squeezing, $g_m = \text{sign}(c_m)$ is needed. The same solution as in Eq. A14 for the optimum parameters is then derived.

The above analysis applies to an ideal lossless situation. In a practical scenario, however, loss $1 - \eta$ is present at each sensor. Effectively, loss can be accounted for at the source by replacing Eq. A10 with

$$\langle \text{Im}[\hat{b}]^2 \rangle = \frac{1}{4} \left[\frac{\eta}{(\sqrt{N_S} + \sqrt{N_S + 1})^2} + (1 - \eta) \right], \quad (\text{A17})$$

where η is the transmissivity. The optimum solutions in Eq. A14 and Eq. A15, as well as the variance in Eq. A16 remains valid with $\beta = \sqrt{\eta} \sqrt{2}J_1(A_m)\alpha$.

3. Performance analysis

To compare the performance of quantum sensing protocols, one should first identify resource constraints. Various theoretical works simply consider an energy constraint, i.e., by fixing the total mean photon numbers employed in different protocols under comparison. The energy constraint is valid in scenarios where the interrogated sample is sensitive to the probe power caused by, e.g., photodamage or self-concealing. In RF-photonics sensing and LIGO, however, the optical power should ideally be cranked up as much as one can until the device power accommodation limit is arrived. Therefore, in an RF-photonics sensor, the power carried by the central mode \hat{a}_c needs be large, subject to the operational limit of the device. For example, integrated RF-photonics sen-

sors can accommodate milliwatts of optical power [23]. In a classical separable RF-photonic sensor network, the effective mode \hat{b} is in a vacuum state, and the laser power distribution to different sensors is optimized through tuning the beam-splitter ratios.

In an entangled RF-photonic sensor network, phase squeezed light resides in the effective mode \hat{b} . Because the experimental energy the squeezed state $N_S \ll |\alpha|^2$, it is negligible, as compared to that of the central spectral mode. As such, the performance comparison between the classical separable and entangled sensor networks is based on setting the classical scheme's \hat{b} in a vacuum state and the entangled scheme's \hat{b} to a squeezed state while employing identical energies on the central spectral modes for both cases. The estimation variances for both schemes are modeled by Eq. A15, with $\langle \text{Im}[\hat{b}]^2 \rangle$ given in Eq. A17 for the entangled sensor network and $\langle \text{Im}[\hat{b}]^2 \rangle = 1/4$ for the classical separable sensor network.

To show that the quantum state shared by the sensors is indeed entangled, we performed a theoretical comparison between the DQS scheme and the optimum separable scheme, subject to a total photon number constraint in the \hat{b}_m modes for both cases. As analyzed in Ref. [18, 22], in the absence of loss, the optimum separable DQS utilizes $\{\hat{b}^{(m)}, 1 \leq m \leq M\}$ modes in a product of squeezed vacuums, with the optimum mean photon number distribution $N_S^{(m)}$ under the constraint $\sum_{m=1}^M N_S^{(m)} = N_S$. Suppose the same beam splitter array is used to distribute the central spectral mode's coherent state to different sensors, the unbiased estimator condition remains the same as Eq. A13. Now, the $\hat{b}^{(m) \prime}$ modes are separable, each having a variance of

$$\text{var}(\text{Im}[\hat{b}^{(m) \prime}]) = \frac{1}{4} \left[\frac{\eta}{(\sqrt{N_S^{(m)}} + \sqrt{N_S^{(m)} + 1})^2} + (1 - \eta) \right]. \quad (\text{A18})$$

Akin to Eq. A16, the estimation variance

$$\text{var}(\hat{L}) = \sum_{m=1}^M \frac{c_m^2}{w_m^2 \beta^2} \text{var}(\text{Im}[\hat{b}^{(m) \prime}]). \quad (\text{A19})$$

For a set of fixed w_m 's, one optimizes $N_S^{(m)}$ to minimize the estimation variance. One can show the overall minimum is achieved at $w_m^2 \propto c_m \sqrt{\text{var}(\text{Im}[\hat{b}^{(m) \prime}])}$:

$$\text{var}(\hat{L})^* = \min_{\sum_m N_S^{(m)} = N_S} \sum_{m=1}^M \frac{c_m}{\beta} \sqrt{\text{var}(\text{Im}[\hat{b}^{(m) \prime}])}. \quad (\text{A20})$$

In our experiment, at the source we measured the anti-

squeezing level as ~ 10 dB above the shot-noise level and the squeezing level as ~ 4 dB below the shot-noise level, from which we can infer the ideal source squeezing as ~ 11.7 dB and mean photon number $N_S \sim 3.3$. In the field amplitude measurement, the measured squeezing was ~ 3.2 dB (noise variance ~ 0.48 of that of the shot noise) for the three sensor network case. Thus, the overall efficiency $\eta \sim 0.56$ are then derived. With equal weights, the optimum separable scheme employs ~ 7.9 dB of squeezing at the local source, to match the total mean photon number in squeezing, and achieves a 2.7 dB of noise reduction (noise variance ~ 0.53 of the shot noise). This leads to a $\sim 10\%$ advantage in estimation variance for our experimental result over that of the optimum separable sensor network, thereby verifying the entanglement shared by the sensors.

It is worth noting that the optimum separable RF-photonic sensor network discussed above requires that each sensor has its own squeezed-light source, which induces a substantial resource overhead.

4. Finite difference method for the estimation of AoA of the RF field

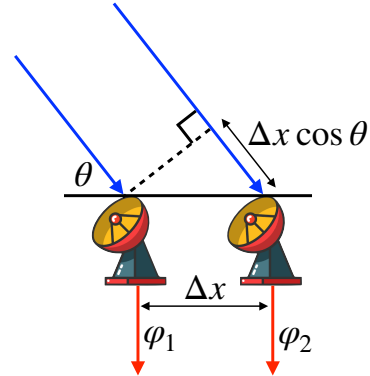


FIG. 6. A simple scheme to estimate the AoA of an incident RF field based on phase difference ($\varphi_2 - \varphi_1$) measurement at two RF sensors. Dashed line is the wavefront of the RF field.

A simple example of measuring the AoA of an incident RF field is illustrated in Fig. 6. The AoA θ is related to the relative phase of the two sensors by

$$\frac{\varphi_2 - \varphi_1}{2\pi} = \frac{\Delta x \cos \theta}{\lambda} + k, \quad (\text{A21})$$

where λ is the wavelength of the RF field, and k is an integer. k can be set to 0, if the sensors are located close to a less than a wavelength, i.e., $\Delta x/\lambda \ll 1$, but the measurement of the AoA, in general, is not restricted to this

assumption. The AoA can then be estimated as

$$\theta = \arccos \frac{(\varphi_2 - \varphi_1)\lambda}{2\pi\Delta x}. \quad (\text{A22})$$

Since both λ and Δx are predetermined, the measurement of the AoA of an RF field is transformed into a difference phase estimation problem undertaken by the two sensors, which is a focus of the present article. Now we characterize the discretization error and optimize the precision of phase-difference estimation.

We will consider the three-point case, $x_1 < x_2 < x_3$, suppose the weights are c_1, c_2, c_3 . The estimator is

$$\hat{L} = c_1\varphi(x_1) + c_2\varphi(x_2) + c_3\varphi(x_3). \quad (\text{A23})$$

Case 1.— Phase-difference estimation at a central node.

$$\begin{aligned} \varphi(x_1) &= \varphi(x_2) - \varphi^{(1)}(x_2)\Delta x + \frac{1}{2}\varphi^{(2)}(x_2)\Delta x^2 + O(\Delta x^3), \\ \varphi(x_3) &= \varphi(x_2) + \varphi^{(1)}(x_2)\Delta x + \frac{1}{2}\varphi^{(2)}(x_2)\Delta x^2 + O(\Delta x^3). \end{aligned} \quad (\text{A24})$$

One requires $c_3 = 1 + c_1, c_2 = -1 - 2c_1$ to ensure the expectation value $\langle \hat{L} \rangle = \varphi^{(1)}(x_2)\Delta x + O(\Delta x^2)$. In particular if we require $c_1 + c_3 = 0$, or $(c_1, c_2, c_3) = (-1/2, 0, 1/2)$, then $\langle \hat{L} \rangle = \varphi^{(1)}(x_2)\Delta x + O(\Delta x^3)$.

With the proper chosen weights in Eq. A14, the variance in Eq. A15 is

$$\text{var}(\hat{L}) = \left(\sum |c_m|/\beta \right)^2 \langle \text{Re} \hat{b}^2 \rangle \propto (|c_1| + |1 + 2c_1| + |1 + c_1|)^2. \quad (\text{A25})$$

It is minimized when $c_1 = -1/2$. Thus, it is always optimum to use $(c_1, c_2, c_3) = (-1/2, 0, 1/2)$, because this minimizes both the estimation variance and the discretization error for the phase gradient.

Case 2.— Phase-difference estimation at an edge node.

$$\begin{aligned} \varphi(x_2) &= \varphi(x_1) + \varphi^{(1)}(x_1)\Delta x + \frac{1}{2}\varphi^{(2)}(x_1)\Delta x^2 + O(\Delta x^3), \\ \varphi(x_3) &= \varphi(x_1) + \varphi^{(1)}(x_1)2\Delta x + \frac{1}{2}\varphi^{(2)}(x_1)4\Delta x^2 + O(\Delta x^3). \end{aligned} \quad (\text{A26})$$

One requires $c_2 = 1 - 2c_3, c_1 = c_3 - 1$ to ensure the expectation value $\langle \hat{L} \rangle = \varphi^{(1)}(x_1)\Delta x + O(\Delta x^2)$. If $c_2 + 4c_3 = 0$ is required, then $(c_1, c_2, c_3) = (-3/2, 2, -1/2)$ and $\langle \hat{L} \rangle = \varphi^{(1)}(x_1)\Delta x + O(\Delta x^3)$.

A similar analysis can be performed for the second-order derivative, except that there is only one possible set of parameters for each case. To estimate at a central node, one needs $c_1 = c_3 = 1/2, c_2 = -1$, so $\langle \hat{L} \rangle = \varphi^{(2)}(x_2)\Delta x^2 + O(\Delta x^4)$. To estimate at an edge

node, one needs $c_1 = 1, c_2 = -2, c_3 = 1$, so $\langle \hat{L} \rangle = \varphi^{(2)}(x_1)\Delta x^2 + O(\Delta x^3)$.

Appendix B: Experimental Details

A detailed experimental diagram is drawn in Fig. 7. A 1550-nm mode-hop-free semiconductor laser (New Focus Velocity TLB-6728) generates ~ 10 mW of light, which is modulated by a fiber-based phase modulator (PM) driven by a 24-MHz signal to create two sidebands for cavity locking based on the Pound-Drever-Hall (PDH) technique. The modulated light is subsequently boosted to ~ 1 W by an erbium-doped fiber amplifier (EDFA) and coupled to free space. The 1550-nm light is first filtered by a locked 1550-nm mode-cleaning cavity (MC) and then split into two arms to serve, respectively, as the pump for second-harmonic generation (SHG) and the LO for homodyne measurements. The semi-monolithic SHG cavity entails a curved cavity mirror with 10% reflectivity at 775 nm and 94% reflectivity at 1550 nm [28] and a type-0 periodically-poled KTiOPO₄ (PPKTP) crystal temperature stabilized at 34.0°C. The PPKTP crystal has a curved facet being highly reflective at 1550 nm and 775 nm and a flat facet that is anti-reflection coated at both wavelengths. The SHG cavity is locked using the 24-MHz sideband and generates ~ 300 mW of 775-nm light under a 500-mW 1550-nm pump. The 775-nm light is first filtered by a locked 775-nm MC and then injected through a curved cavity mirror into an OPA cavity where a second identical PPKTP crystal temperature stabilized at 40.5°C is embedded. The curved mirror of the OPA cavity has 95% reflectivity at 775 nm and 87.5% reflectivity at 1550 nm. To generate phase squeezed light, a weak 1550-nm beam is tapped from the LO and modulated by a free-space PM to create 20-MHz sidebands. The modulated weak 1550-nm beam is reflected on a 775-nm/1550-nm dichroic beam splitter (DBS) and then seeds the OPA cavity. The OPA cavity is locked by the 24-MHz sideband of the 775-nm light that transmits through the DBS. 2% of the 1550-nm output from the OPA curved cavity mirror is tapped and is employed to lock the phase between the 1550-nm seed beam and the 775-nm pump using the 20-MHz sidebands so that the OPA operates in a parametric amplification regime. When phase locked, the OPA cavity emits quantum light composed of an effective squeezed vacuum state residing in the 11-MHz sideband modes while the central spectral mode is a displaced phase squeezed state. Due to the large quadrature displacement, the central spectral mode can be well approximated by a classical coherent state. The single spatial-mode quantum light is diverted into three RF-photon sensors by two VBSs, each consisting of a half-

- [10] S.-H. Tan, B. I. Erkmen, V. Giovannetti, S. Guha, S. Lloyd, L. Maccone, S. Pirandola, and J. H. Shapiro, Quantum illumination with Gaussian states, *Phys. Rev. Lett.* **101**, 253601 (2008).
- [11] E. D. Lopaeva, I. Ruo Berchera, I. P. Degiovanni, S. Olivares, G. Brida, and M. Genovese, Experimental realization of quantum illumination, *Phys. Rev. Lett.* **110**, 153603 (2013).
- [12] Q. Zhuang, Z. Zhang and J. H. Shapiro, Optimum mixed-state discrimination for noisy entanglement-enhanced sensing, *Phys. Rev. Lett.* **118**, 040801 (2017)
- [13] S. Barzanjeh, S. Guha, C. Weedbrook, D. Vitali, J. H. Shapiro, and S. Pirandola, Microwave quantum illumination, *Phys. Rev. Lett.* **114**, 080503 (2015).
- [14] S. Barzanjeh, S. Pirandola, D. Vitali, and J. M. Fink, Experimental microwave quantum illumination, *arXiv:1908.03058*.
- [15] D. Marpaung, J. Yao, and J. Capmany, Integrated microwave photonics, *Nature Photon.* **13**, 80–90 (2019).
- [16] P. Ghelfi *et al.*, A fully photonics-based coherent radar system, *Nature* **507**, 341–345 (2014).
- [17] C. Lim *et al.*, Fiber-wireless networks and subsystem technologies, *J. Lightw. Technol.* **28**, 390–405 (2010).
- [18] Q. Zhuang, Z. Zhang, and J. H. Shapiro, Distributed quantum sensing using continuous-variable multipartite entanglement, *Phys. Rev. A* **97**, 032329 (2018).
- [19] T. J. Proctor, P. A. Knott, and J. A. Dunningham, Multiparameter estimation in networked quantum sensors, *Phys. Rev. Lett.* **120**, 080501 (2018).
- [20] W. Ge, K. Jacobs, Z. Eldredge, A. V. Gorshkov, and M. Foss-Feig, Distributed quantum metrology with linear networks and separable inputs, *Phys. Rev. Lett.* **121**, 043604 (2018).
- [21] X. Guo *et al.*, Distributed quantum sensing in a continuous variable entangled network, *arXiv:1905.09408*.
- [22] Y. Xia, Q. Zhuang, W. Clark, and Z. Zhang, Repeater-enhanced distributed quantum sensing based on continuous-variable multipartite entanglement, *Phys. Rev. A* **99**, 012328 (2019).
- [23] W. Jiang *et al.*, Efficient bidirectional piezo-optomechanical transduction between microwave and optical frequency, *arXiv:1909.04627*.
- [24] Z. Qin, M. Gessner, Z. Ren, X. Deng, D. Han, W. Li, X. Su, A. Smerzi, and K. Peng, Characterizing the multipartite continuous-variable entanglement structure from squeezing coefficients and the Fisher information, *npj Quantum Inf.* **5**, 3, (2019)
- [25] Q. Zhuang and Z. Zhang, Physical-layer supervised learning assisted by an entangled sensor network, *arXiv:1901.09566*, to appear in *Phys. Rev. X*.
- [26] T. C. Ralph and A. P. Lund, in *Proceedings of the Ninth International Conference on Quantum Communication, Measurement and Computing*, Calgary, 2008, edited by A. Lvovsky, (AIP, 2009), p. 155.
- [27] K. Noh, S. M. Girvin, and L. Jiang, Encoding an oscillator into many oscillators, *arXiv:1903.12615*.
- [28] M. Mehmet, S. Ast, T. Eberle, S. Steinlechner, H. Vahlbruch, and R. Schnabel, Squeezed light at 1550 nm with a quantum noise reduction of 12.3 dB, *Opt Express.* **19**, 25763 (2011).
- [29] K. Qian, Z. Eldredge, W. Ge, G. Pagano, C. Monroe, J. V. Porto, and A. V. Gorshkov, Heisenberg-scaling measurement protocol for analytic functions with quantum sensor networks, *arXiv 1901.09042*.